GeSn optical gain and lasing characteristics modelling

Quang Minh Thai [1,*] Jeremie Chretien,[1] Mathieu Bertrand,[2] Lara Casiez,[2] Alexei Chelnokov [2]
Vincent Reboud,[2] Nicolas Pauc,[1] and Vincent Calvo[1]
[1]*University Grenoble Alpes, CEA, IRIG-Pheliqs, 38000 Grenoble, France*
[2]*University Grenoble Alpes, CEA, Leti, 38000 Grenoble, France*

With recent demonstrations of lasing, germanium-tin (GeSn) stands out as a promising candidate for the integration of a low threshold, room temperature monolithic laser source in silicon (Si) photonics. The impact of physical properties, such as energy band structure, crystal quality, and cavity loss on lasing performances (i.e., lasing threshold and maximal lasing temperature) has to be better understood, however. In this work, we calculate the theoretical band-to-band net gain for relaxed, [100] uniaxial, and (100) biaxial tensile-strained GeSn. We show that the band-to-band net gain depends not only on the interband gain introduced by the transition between valence bands and conduction bands, but also on the intervalence band absorption between the valence bands. Both approaches, GeSn with high Sn concentration and/or with high tensile strain, can yield a band-to-band net gain at room temperature. Then, the integration of another source of absorption—free carrier absorption— will be discussed. Finally, from the simulation of GeSn lasing characteristics, we show the important role the crystal quality has on the lasing threshold. Based on the results, we suggest using GeSn with low/medium Sn concentrations, under very high [100] uniaxial or (100) biaxial tensile strain, to obtain a low threshold, room temperature lasers.

I. INTRODUCTION

Interests in a monolithically integrated laser source for silicon (Si) photonics increased recently, with the experimental demonstrations of lasing in germanium-tin (GeSn) alloys [1–4] and strained Ge [5–7]. In the case of GeSn, several experimental studies were conducted to optimize its lasing performance, i.e., reduce the lasing threshold and increase the maximal lasing temperature. Various strategies were tested, including different types of microcavities (Fabry-Perot waveguide [1,3,8–11], microdisk [2,4,11–15], photonic-crystal [16], microbridge [17]), different Sn concentrations—between 5.4% and 20%, multiquantum wells [9,12] and the application of (100) biaxial [14,15] or [100] uniaxial tensile strain [17]. Two trends were identified based on experimental results: the lasing threshold decreased when the Sn concentration decreased—down to $0.8 \, \text{kW/cm}^2$ in a microdisk with 5.4% of Sn at 25 K (we will call it "GeSn 5.4%" from now on), under (100) biaxial tensile strain [15]. Meanwhile, the maximum lasing temperature increased when the Sn concentration and/or the applied strain increased, with current records at 270 and 273 K for a GeSn Fabry-Perot waveguide up to 20% of Sn [10] and a suspended GeSn 16.0% microbridge under [100] uniaxial tensile strain [17], respectively.

So far, only a few theoretical studies of GeSn and strained Ge lasers—in terms of optical gain and resolution of the laser equations—can be found in the literature. Rainko *et al.* calculated the net optical gain of (100) biaxial-tensile-strained GeSn, taking into account the interband gain from the transition between the valence band and the condition band, and the free carrier absorption (FCA) [18]. Intervalence band absorption (IVBA) was also suggested as an additional mechanism limiting the net optical gain [19–22]. Early works of Geiger [19], Suess *et al.* [20], and Carroll *et al.* [21] provided an empirical, linear expression of IVBA as a function of the photon energy. Gupta *et al.* [22] calculated IVBA and FCA for [100] uniaxial strained Ge, with IVBA extracted solely from the band structure of the material. It showed a more complex IVBA profile, compared to the linear empirical expression. The authors pointed out the important role of intervalence transition between two valence bands, and between the spin-orbit band and the valence bands. It is thus interesting to study the impact of IVBA and FCA on the optical gain of GeSn, for different values of Sn concentration and applied strain. In addition, the lasing threshold of GeSn depends on various factors, for example, the crystal quality: this effect is quantified using the nonradiative lifetime, describing how long the electrons and holes can stay in their excited states, before combining through an intermediate trap level. The cavity loss is another important factor to consider. A detailed analysis of those two parameters using laser equations [23] is therefore necessary to better understand the performance of GeSn lasers.

We will present in Sec. II the methodology adopted to calculate the band-to-band optical gain and the lasing characteristics of GeSn. We will calculate in Sec. III the net
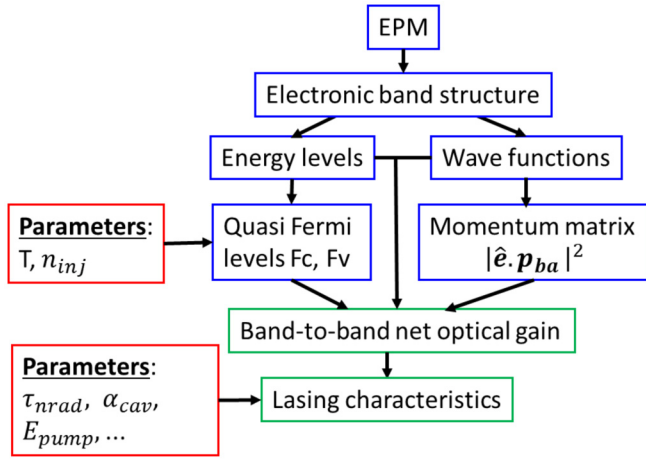
*thaiquangminh1993@gmail.com

FIG. 1. The simulation workflow for the calculation of the band-to-band net optical gain and the lasing characteristics of GeSn.

band-to-band optical gain, first for relaxed GeSn with different Sn concentrations, between 25 and 298 K, then for (100) biaxial and [100] uniaxial tensile strained GeSn at 298 K. We will discuss in Sec. IV the integration of FCA in the calculation of net gain. Finally, in Sec. V, we will show the impact of nonradiative lifetime and cavity loss on the lasing threshold of GeSn optical cavity, by solving the laser equations.

II. METHODOLOGY

A. Simulation workflow

For a given GeSn configuration (Sn concentration, applied strain), we first calculate its band structure using the local empirical pseudopotential method (EPM) [24,25]. Then, using the calculated energy levels and the wave functions, we establish a relationship between the injected carrier density and the quasi-Fermi levels (for electrons and holes, respectively), plus the momentum matrix. With these data, we calculate the band-to-band net optical gain of GeSn and finally, the lasing characteristics of the GeSn laser. The simulation workflow is shown in Fig. 1. The methodology adopted for FCA calculation will be detailed in Sec. IV.

B. Electronic band structure of GeSn

In local EPM, the Hamiltonian is written as

$$H(\boldsymbol{G}, \boldsymbol{G}') = -\frac{\hbar^2}{2m}\Delta + V_{\text{loc}}(\boldsymbol{G} - \boldsymbol{G}') + V_{\text{SO}}(\boldsymbol{G}, \boldsymbol{G}'), \quad (1)$$

where $-\frac{\hbar^2}{2m}\Delta$, $V_{\text{loc}}(\boldsymbol{G} - \boldsymbol{G}')$, and $V_{\text{SO}}(\boldsymbol{G}, \boldsymbol{G}')$ are, respectively, the kinetic term, the local pseudopotential, and the spin-orbit pseudopotential. The formula giving V_{loc} and V_{SO} are as follows [25]:

$$V_{\text{loc}}(\boldsymbol{G} - \boldsymbol{G}') = S(\boldsymbol{G} - \boldsymbol{G}')V(|\boldsymbol{G} - \boldsymbol{G}'|)$$

$$= \left(\frac{1}{N_{\text{at}}}\sum_{\text{at}} e^{[-i(\boldsymbol{G}-\boldsymbol{G}')\boldsymbol{r}_{\text{at}}]}\right)V(|\boldsymbol{G} - \boldsymbol{G}'|), \quad (2)$$

$$V_{\text{SO}}(\boldsymbol{G}, \boldsymbol{G}') = -2i\mu_{\text{SO}}\left(\frac{(\Omega/2)^{1/3}}{\pi}\right)^2 S(\boldsymbol{G} - \boldsymbol{G}')$$

$$B(|\boldsymbol{G}|)B(|\boldsymbol{G}'|)(\boldsymbol{G} \times \boldsymbol{G}')\cdot <\sigma|\boldsymbol{S}|\sigma'>, \quad (3)$$

with

$$B(|\boldsymbol{G}|) = \frac{5 - (G/\varsigma)^2}{5[1 + (G/\varsigma)^2]^4}, \quad (4)$$

where N_{at}, $\boldsymbol{r}_{\text{at}}$, Ω, S, and $B(|\boldsymbol{G}|)$ are the number and the coordinates of atoms in the primitive cell, the volume of the primitive cell, the Pauli vector, and the overlap integral, respectively. The local form factors $V(|\boldsymbol{G} - \boldsymbol{G}'|)$ and the spin-orbit parameters μ_{SO}, ς are variables that are optimized to fit the energy gaps of GeSn.

In unstrained GeSn with a diamond crystal structure, values of V are required only when $|\boldsymbol{G} - \boldsymbol{G}'|_{\text{relax}} = \{\sqrt{3}, \sqrt{8}, \sqrt{11}\}\frac{2\pi}{a_0}$. These values will be denoted V_3, V_8, V_{11}. For strained GeSn, we apply a spline interpolation to extract V at an arbitrary value of $|\boldsymbol{G} - \boldsymbol{G}'|$. To obtain a good interpolation, we define, for each special value of $|\boldsymbol{G} - \boldsymbol{G}'|_{\text{relax}}$, two neighbored values of V to determine the slope of the curve. We call these values V^-, V, V^+, corresponding to the wave vectors $q^- = \frac{1}{1+\theta}|\boldsymbol{G} - \boldsymbol{G}'|_{\text{relax}}$, $q = |\boldsymbol{G} - \boldsymbol{G}'|_{\text{relax}}$, $q^+ = \frac{1}{1-\theta}|\boldsymbol{G} - \boldsymbol{G}'|_{\text{relax}}$. The cutoff of the plane wave basis is taken as $|\boldsymbol{G}|_{\text{cutoff}} = 3.8\frac{2\pi}{a_0}$. V is set to 0 when $|\boldsymbol{G}| = 0$ or $|\boldsymbol{G}| = |\boldsymbol{G}|_{\text{cutoff}}$.

We fit the pseudopotential to reproduce the reference values of the direct, the indirect, and the spin-orbit gap of GeSn. In relaxed GeSn, they are taken from 8-band k.p modeling
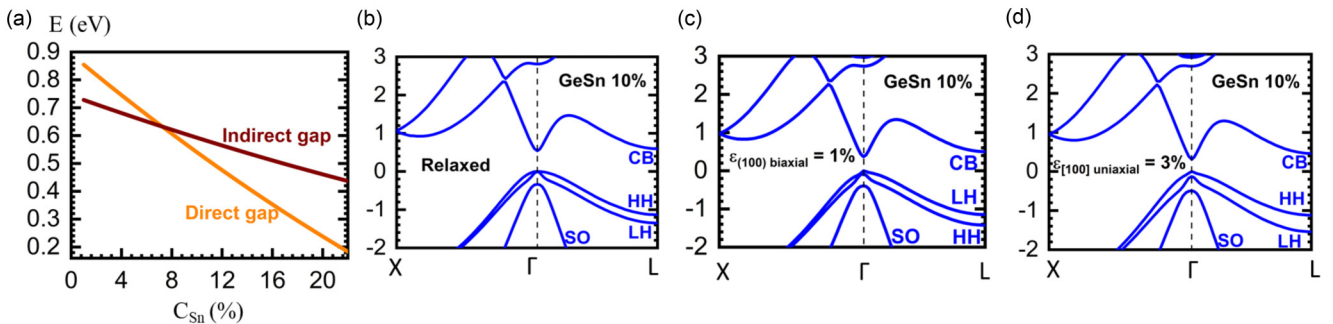

FIG. 2. (a) Direct and indirect gaps of relaxed GeSn, as a function of the Sn concentration at 0 K (from Ref. [26]). (b)–(d) Band structure of relaxed GeSn 10%, 1% (100) biaxial strain GeSn 10%, and 3% [100] uniaxial strain GeSn 10%. Here, CB, HH, LH, and SO denote the conduction band, the heavy hole/light hole valence band, and the spin-orbit band.

TABLE I. Deformation potentials, spin-orbit gap, lattice parameter, and elastic constants of Ge and α-Sn. "-" represents a lack of data.

	Ge	α-Sn
$a_{c\Gamma} - a_v$ (eV)	−9.48 [27]	−
$a_{cL} - a_v$ (eV)	−2.78 [27]	−
b (eV)	−2.55 [27]	−
E_{SO} (eV)	0.29 [19]	0.80 [19]
a_0 (Å)	5.6580 [19]	6.4892 [19]
$C11$ (GPa)	129.0 [19]	69.0 [19]
$C12$ (GPa)	48.0 [19]	29.0 [19]

at 0 K [26] [Fig. 2(a)]. In strained GeSn, these values are calculated using the deformation potential theory [27]. Due to the lack of reliable data on deformation potentials $a_{c\Gamma} - a_v$, $a_{cL} - a_v$, b for the diamond phase α-Sn, we use the same deformation potentials of Ge in Ref. [27] for all Sn concentrations. The spin-orbit gap E_{SO}, the lattice parameter a_0, and the elastic constants $C11$, $C12$ are interpolated between Ge and Sn. These parameters are given in Table I.

Since the pseudopotential form is arbitrary, it cannot reproduce simultaneously the gap variation under (100) biaxial strain and [100] uniaxial strain, using a single set of parameters. Therefore, for a given Sn concentration, we fit the pseudopotential for each type of strain to guarantee a good superposition between EPM gaps and the references. The fitted parameters of the pseudopotential for different GeSn cases are given in Table II. We keep $\varsigma = 10.09\,\text{Å}^{-1}$ (value taken from Ref. [22]) in all cases since we observe that changing this parameter has little effect on the band structure of GeSn.

We show in Figs. 2(b) to 2(d) band structures for relaxed GeSn 10%, (100) biaxial, and [100] uniaxial strained GeSn 10%. Energy gaps for strained GeSn 6%, 10%, and 13% at 0 K are shown in Fig. 3.

Because of the lack of experimental Varshni relations within a large range of Sn concentration, for GeSn gain calculations at different temperatures, we use their energy gaps at 0 K.

To validate the calculated band structure, we compared the effective masses and the intrinsic carrier density n_i at 298 K with literature values for pure, unstrained Ge. Table III results are in good agreement with the reference values.

C. Gain formula

The band-to-band optical absorption between two energy bands a and b is [33]

$$\alpha(\hbar\omega) = \frac{\pi e^2}{n_r c \varepsilon_0 m_0^2 \omega} \int_{k \in \text{BZ}} \frac{d^3 k}{(2\pi)^3} \sum_a \sum_b |\hat{\boldsymbol{e}} \cdot \boldsymbol{p}_{ba}|^2$$
$$\delta(E_b(k) - E_a(k) - \hbar\omega)(f_a - f_b), \quad (5)$$

with $\hat{\boldsymbol{e}}$ the polarization of light, $\boldsymbol{p}$ the momentum operator, $|\hat{\boldsymbol{e}} \cdot \boldsymbol{p}_{ba}|^2$ the momentum matrix element, and f the Fermi-Dirac distribution. The refractive index n_r is taken as 4.22 for GeSn [34]. There are two contributions to the band-to-band optical absorption (Fig. 4): interband transition (a is a valence band, while b is a conduction band) and intervalence transition (both a and b are valence bands). The interconduction transition (both a and b are conduction bands) is negligible due to the very high gap between the first and other conduction bands. The integral is transformed into a discrete sum on the first Brillouin zone (BZ), using a Monkhorst-Pack

TABLE II. Fitted pseudopotential parameters for different GeSn configurations studied here. "uni" stands for [100] uniaxial tensile strained GeSn, while "bi" represents (100) biaxial tensile-strained GeSn.

	Relaxed GeSn				
	0% Sn (Ge)	16% Sn	18% Sn	20% Sn	22% Sn
V_3 (Ry)	−0.25319	−0.25520	−0.25103	−0.25207	−0.25141
V_8 (Ry)	0.03486	0.03509	0.03079	0.03203	0.03172
V_{11} (Ry)	0.03626	0.02694	0.02920	0.02726	0.02646
μ_{SO} (Ry)	0.00043	0.00054	0.00055	0.00057	0.00056
ς (Å^{-1})	10.09	10.09	10.09	10.09	10.09

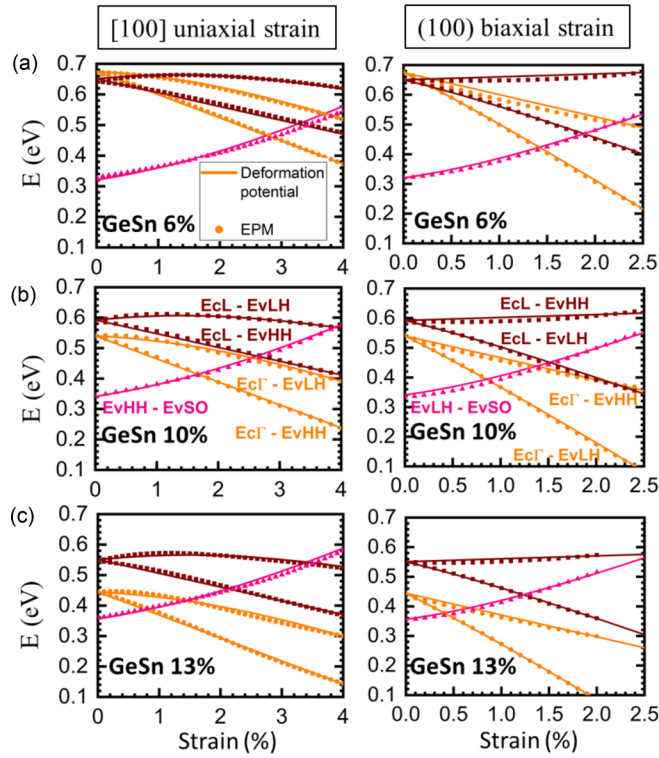|	Strained GeSn					
	6% Sn uni	6% Sn uni bi	10% Sn uni	10% Sn bi	13% Sn uni	13% Sn bi
θ	0.020	0.015	0.015	0.012	0.020	0.012
V_3^- (Ry)	−0.26636	−0.25979	−0.26580	−0.25751	−0.26787	−0.25884
V_3 (Ry)	−0.25412	−0.25125	−0.25183	−0.25020	−0.24984	−0.24968
V_3^+ (Ry)	−0.24717	−0.24875	−0.24777	−0.25319	−0.24098	−0.25077
V_8^- (Ry)	0.03014	0.03289	0.03112	0.03163	0.02960	0.03265
V_8 (Ry)	0.03445	0.03101	0.03171	0.02979	0.02963	0.02913
V_8^+ (Ry)	0.03805	0.03910	0.03589	0.03700	0.03672	0.03407
V_{11}^- (Ry)	0.03014	0.02919	0.03006	0.02885	0.02904	0.02657
V_{11} (Ry)	0.03281	0.03558	0.03269	0.03420	0.03268	0.03309
V_{11}^+ (Ry)	0.03246	0.03756	0.02835	0.03599	0.02491	0.03655
μ_{SO} (Ry)	0.00048	0.00047	0.00050	0.00048	0.00052	0.00051
ς (Å^{-1})	10.09	10.09	10.09	10.09	10.09	10.09

FIG. 3. Energy gaps as a function of [100] uniaxial strain (left) and (100) biaxial strain (right) at $T = 0$ K for (a) GeSn 6%, (b) GeSn 10%, and (c) GeSn 13%. Straight lines are the gaps calculated using the deformation potential theory, while dots are the gaps fitted with EPM. The definition of each curve is shown in (b)

TABLE III. Comparison of the effective masses and the intrinsic carrier density of Ge between calculations with EPM and reference values. Here the well-known Varshni relation for Ge [32] is added to correct the band structure of Ge at 298 K.

	Ge	
	EPM	Reference
m^{l}_{L-CB}	1.527	1.590 [28]
m^{t}_{L-CB}	0.091	0.081 [28]
$m_{\Gamma-CB}$	0.048	0.041 [28]
$m^{[111]}_{\Gamma-HH}$	0.669	0.597 [29]
		0.623 [30]
$m^{[110]}_{\Gamma-HH}$	0.497	0.439 [29]
		0.467 [30]
$m^{[100]}_{\Gamma-HH}$	0.257	0.226 [29]
		0.251 [30]
$m^{[111]}_{\Gamma-LH}$	0.054	0.046 [29]
		0.052 [30]
$m^{[110]}_{\Gamma-LH}$	0.056	0.048 [29]
		0.053 [30]
$m^{[100]}_{\Gamma-LH}$	0.062	0.053 [29]
		0.060 [30]
n_i (cm^{-3}) (at 298 K)	2.9×10^{13}	2.4×10^{13} [31]

(MP) grid [35] with a $200 \times 200 \times 200$ resolution to ensure a convergence of the result.

To approximate the Dirac distribution $\delta[E_b(k) - E_a(k) - \hbar\omega]$, we use a Gaussian function with a full width at half maximum (FWHM) of 40 meV. We observe that this choice of FWHM leads to an underestimation of the transparency threshold of interband/intervalence band absorption, 20–25 meV lower than the value of the direct gap/valence gaps. A narrower Gaussian function can reduce this underestimation, with the cost of higher simulation time since we must increase the resolution of the MP grid to maintain the convergence of the results. However, since the energy offset is
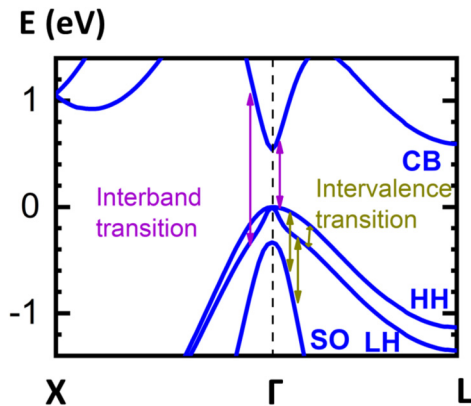

FIG. 4. Optical transition scheme in GeSn.

very small, this approximation does not have a strong impact on results.

In this case, only band-to-band transitions are considered, the net absorption is then the sum of the interband absorption and IVBA. From Eq. (5), $\alpha(\hbar\omega) < 0$ represents an optical gain, while $\alpha(\hbar\omega) > 0$ represents an optical absorption. This convention must be used to interpret all optical gain/absorption curves in the following.

In the next sections, when the interband absorption or the net absorption is negative, we will use, respectively, the term *interband gain* and *net gain*. However, when discussing the numeric results of optical gain, we will use their absolute value to stay coherent with the usual convention, used by the scientific community.

D. Quasi-Fermi levels and momentum matrix elements

The quasi-Fermi levels Fc (for electrons) and Fv (for holes) are calculated for each value of injected carrier density n_{inj} using the following formulas:

$$n = \int_{\substack{k\epsilon\text{BZ}\\a\epsilon\text{CB}}} \frac{d^3k}{(2\pi)^3} \frac{1}{1 + e^{\left(\frac{E_a(k)-F_c}{k_BT}\right)}} = n_{\text{inj}} + n_{\text{dop}}, \quad (6)$$

$$p = \int_{\substack{k\epsilon\text{BZ}\\a\epsilon\text{VB}}} \frac{d^3k}{(2\pi)^3} \frac{1}{1 + e^{\left(\frac{F_v-E_a(k)}{k_BT}\right)}} = n_{\text{inj}} + p_{\text{dop}}, \quad (7)$$

with n_{dop}, p_{dop} n-type and p-type doping levels. The same MP grid (from band-to-band gain calculation) is used to transform the integral into a discrete sum.

In strained GeSn, the polarization of light determines the intensity of momentum matrix elements. We plot in Fig. 5, $|\hat{\boldsymbol{e}} \cdot \boldsymbol{p}_{ba}|^2$ for the band-to-band transition between the highest valence band and the lowest conduction band, first at the Γ point as a function of tensile strain, then at the vicinity of the
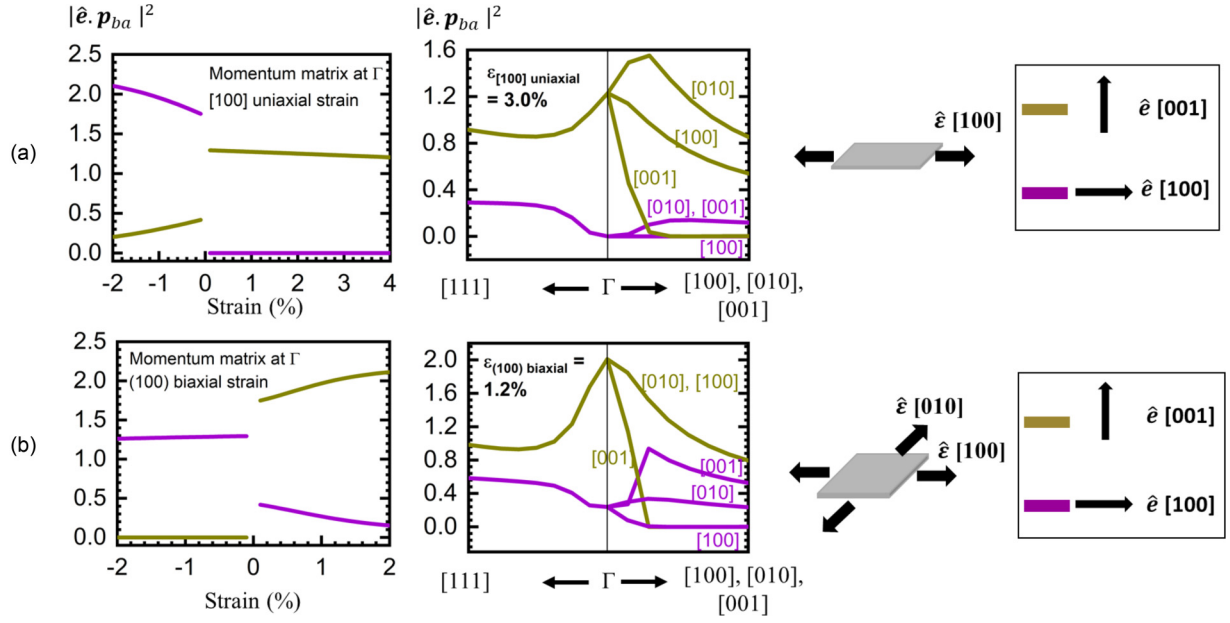
FIG. 5. (a) The variation of $|\hat{e} \cdot \boldsymbol{p}_{ba}|^2$ at the Γ point as a function of applied strain (left), at the vicinity of the Γ point for tensile GeSn (middle), the convention of strain direction, and of light polarization (right) for a) [100] uniaxial strained GeSn 6% and (b) (100) biaxial strained GeSn 6%. Here ε is the applied strain.

Γ point. For both [100] uniaxial [Fig. 5(a)] and (100) biaxial tensile strain [Fig. 5(b)], $|\hat{e} \cdot \boldsymbol{p}_{ba}|^2$ is higher if the light is polarized perpendicularly to the strain direction, which favors both the interband gain and band-to-band net gain. For the rest of the article, we study the optical gain of tensile-strained GeSn only with this polarization of light.

E. Laser equations

The lasing characteristics of a GeSn laser is modelled using the following two equations [23]:

$$G - R_{\text{rad}} - R_{\text{nrad}} - \frac{c}{n_r} g_p S_p = 0, \tag{8}$$

$$\frac{c}{n_r}(\Gamma_p g_p - \alpha_{\text{cav}})S_p + C_{sp}R_{\text{rad}} = 0, \tag{9}$$

with each individual term in Eqs. (8) and (9) written as

$$G = \frac{P_{\text{abs}}}{E_{\text{pump}}(d_1 - d_0)} = \frac{P(e^{-\alpha d_0} - e^{-\alpha d_1})}{E_{\text{pump}}(d_1 - d_0)}, \tag{10}$$

$$R_{\text{rad}} = \beta_{\text{rad}}(n_\Gamma p - n_i^2), \tag{11}$$

$$R_{\text{nrad}} = \frac{n}{\tau_{\text{nrad}}} + C_n n(np - n_i^2) + C_p p(np - n_i^2), \tag{12}$$

$$\alpha_{\text{cav}} = \frac{n_r \omega}{cQ}. \tag{13}$$

The definition and the unit of each parameter are detailed in Table IV.

III. BAND-TO-BAND GAIN CALCULATION FOR GESN

For relaxed GeSn and tensile-strained GeSn, we limit the band-to-band gain calculation to intrinsic, nondoped material.

A. Relaxed GeSn

We calculate the net absorption for relaxed GeSn as a function of Sn concentration and temperature. For each

TABLE IV. Units and definitions of the parameters used in the laser equations. SRH stands for Shockley-Read-Hall mechanism.

Parameter	Unit	Definition
G	cm^{-3} s^{-1}	Carrier generation rate
R_{rad}	cm^{-3} s^{-1}	Radiative recombination rate
R_{nrad}	cm^{-3} s^{-1}	Nonradiative recombination rate (SRH and Auger mechanism)
S_p	cm^{-3}	Emitted photon density in the lasing mode
g_p	cm^{-1}	Net gain (with reversed sign)
α_{cav}	cm^{-1}	Cavity loss of the lasing mode
Γ_p		Optical confinement factor of the lasing mode
C_{sp}		Ratio of spontaneous emission triggering the stimulated emission
E_{pump}	eV	Pump photon energy
α	cm^{-1}	Absorption at the pump photon energy
P	kW cm^{-2}	Pump power
P_{abs}	kW cm^{-2}	Pump power absorbed in the gain medium
d_0, d_1	cm	Initial and final depth of the gain medium
Q		Quality factor of the lasing mode
n_i	cm^{-3}	Intrinsic carrier density
β_{rad}	cm^3 s^{-1}	Radiative recombination coefficient
τ_{nrad}	s	Nonradiative lifetime
C_n, C_p	cm^6 s^{-1}	Auger recombination coefficient for electron (n) and hole (p)

TABLE V. Maximum of the band-to-band net gain (in absolute value) for relaxed GeSn, with n_{inj} between 5×10^{16} cm^{-3} and 3×10^{19} cm^{-3}, as a function of the Sn concentration and the temperature. The gain unit is in cm^{-1}. n_{inj} value (in cm^{-3}) at the maximum net gain is indicated in the parentheses. "–" signifies an absence of net gain.

	25 K	100 K	150 K	220 K	298 K
6% Sn	121	6	–	–	–
	(1×10^{19})	(1×10^{19})			
10% Sn	2675	1802	1106	262	–
	(1×10^{19})	(1×10^{19})	(1×10^{19})	(1×10^{19})	
13% Sn	3013	1803	1224	602	93
	(5×10^{18})	(5×10^{18})	(1×10^{19})	(1×10^{19})	(1×10^{19})
16% Sn	2934	2205	2171	2061	1848
	(5×10^{18})	(3×10^{19})	(3×10^{19})	(3×10^{19})	(3×10^{19})
18% Sn	3874	3726	3607	3381	3018
	(3×10^{19})	(3×10^{19})	(3×10^{19})	(3×10^{19})	(3×10^{19})
20% Sn	4240	4221	4201	4012	3588
	(3×10^{19})	(3×10^{19})	(3×10^{19})	(3×10^{19})	(3×10^{19})
22% Sn	4615	4636	4618	4386	3842
	(1×10^{19})	(3×10^{19})	(3×10^{19})	(3×10^{19})	(3×10^{19})

GeSn configuration, we run the simulation for six injected carrier densities: $n_{inj} = 5 \times 10^{16}$ cm^{-3}, 2×10^{17} cm^{-3}, 1×10^{18} cm^{-3}, 5×10^{18} cm^{-3}, 1×10^{19} cm^{-3}, and 3×10^{19} cm^{-3}, covering the low excitation to the high excitation regime. We extract the maximum of the band-to-band net gain, with the value of n_{inj} at such a maximum, for each GeSn configuration (Table V): When the Sn concentration

increases, the net gain can appear at higher temperature. At room temperature (298 K), the net gain exists from GeSn 13% upward.

We plot in Fig. 6(a) IVBA, interband, and net absorption spectra of GeSn 10%, 13%, 16%, at 298 K, for different values of n_{inj}. As expected, interband gain appears when the photon energy is superior to the direct gap. For relaxed GeSn, there
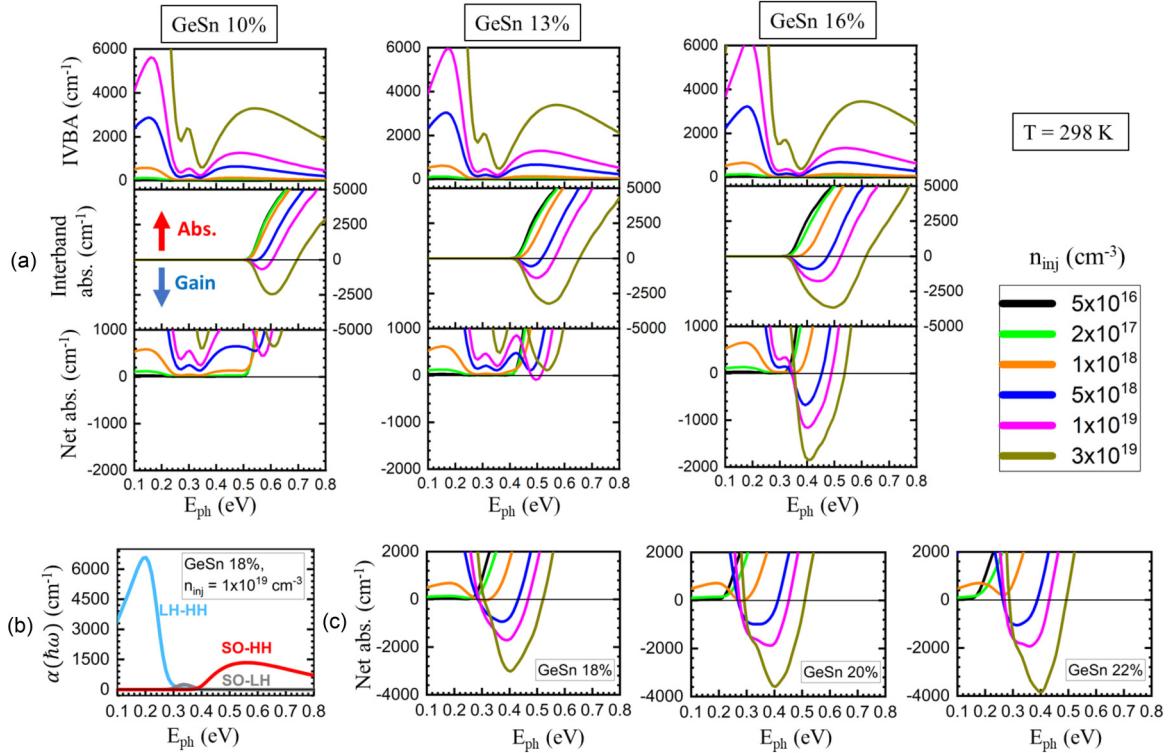

FIG. 6. (a) IVBA, interband, and net absorption spectra for GeSn 10%, 13%, and 16% at 298 K. Sign convention of absorption/gain is indicated in the interband absorption graph of GeSn 10%. (b) Different absorption branches (LH-HH, SO-HH, and SO-LH) of IVBA in relaxed GeSn 18%, for $n_{inj} = 1 \times 10^{19}$ cm^{-3} at 298 K. (c) Net absorption spectra of GeSn 18%, 20%, and 22% at 298 K. The color code for different values of n_{inj} is the same for (a) and (c).
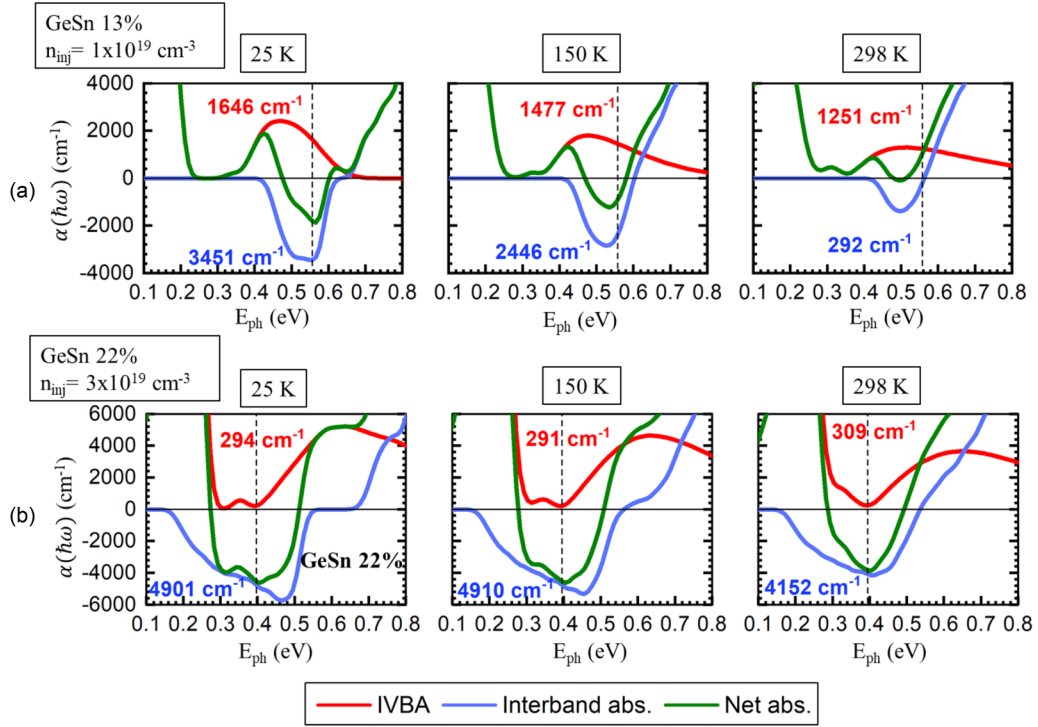
FIG. 7. Evolution of IVBA, interband, and net absorption spectra at 25, 150, and 298 K, (a) with n_{inj} fixed at 1×10^{19} cm^{-3} for GeSn 13% and (b) with n_{inj} fixed at 3×10^{19} cm^{-3} for GeSn 22%.

are two main branches of strong IVBA [Fig. 6(b)]: The first one at low photon energies is due to a transition between the light hole bands and the heavy hole bands (LH-HH), while the second one at higher photon energies comes from the transition between the spin-orbit bands and the heavy hole bands (SO-HH). The curve form of IVBA found in our work agrees very well with Ref. [22] results.

For GeSn 10% and 13%, there is a strong overlap between the interband gain and the SO-HH branch of IVBA. This overlap suppresses the net gain in GeSn 10% at 298 K. In GeSn 13%, thanks to a higher interband gain due to a larger difference between the minimum of the conduction band at Γ and at L $E_{c\Gamma} - E_{cL}$ compared to GeSn 10%, there is a net gain that exists at 298 K. However, its value is limited significantly because of the overlap (capped at 93 cm^{-1}). It is worth noting that, in both cases, a n_{inj} increase does not guarantee that the net gain will be stronger: While the inter-

band gain increases, IVBA increases at the same time, which might result in an even stronger net absorption. This correlated effect from the interband gain and IVBA explains why, in some cases, like GeSn between 6% and 13% Sn concentration, the maximum net gain is located at a medium value of n_{inj} (5×10^{18} cm^{-3} and 1×10^{19} cm^{-3}) instead of the highest value of 3×10^{19} cm^{-3}.

When the Sn concentration increases further than 13%, the direct gap decreases and the spin-orbit gap increases. As a result, it pulls the interband gain and the SO-HH branch of IVBA in opposite directions. A part of the interband gain is now located in the valley between the LH-HH and SO-HH absorption branches, where IVBA is weak. The net gain is thus enhanced significantly in that case. For GeSn 16%, a higher interband gain, due to a larger value of $E_{c\Gamma} - E_{cL}$, together with a weak overlap between IVBA and the interband gain between 0.35 and 0.54 eV, boosts the net gain, resulting

TABLE VI. Maximum of the band-to-band net gain (in cm^{-1}) with the corresponded value of n_{inj} (in parentheses, in cm^{-3}) for [100] uniaxial tensile strained GeSn at 298 K, with n_{inj} between 5×10^{16} cm^{-3} and 3×10^{19} cm^{-3}, as a function of the Sn concentration and the applied strain ε.

	[100] uniaxial tensile strain, $T = 298$ K								
	$\varepsilon = 0\%$	0.5%	1.0%	1.5%	2.0%	2.5%	3.0%	3.5%	4.0%
6% Sn	–	–	–	–	–	–	36	1331	2629
							(1×10^{19})	(1×10^{19})	(3×10^{19})
10% Sn	–	–	–	–	433	1821	2959	3760	3706
					(1×10^{19})	(3×10^{19})	(3×10^{19})	(3×10^{19})	(3×10^{19})
13% Sn	93	209	531	1568	2798	3799	4273	4167	3456
	(1×10^{19})	(1×10^{19})	(1×10^{19})	(3×10^{19})	(3×10^{19})	(3×10^{19})	(3×10^{19})	(3×10^{19})	(3×10^{19})

TABLE VII. Maximum of the band-to-band net gain (in cm^{-1}) with the corresponding value of n_{inj} (in parentheses, in cm^{-3}) for (100) biaxial tensile strained GeSn at 298 K, with n_{inj} between 5×10^{16} cm^{-3} and 3×10^{19} cm^{-3}, as a function of the Sn concentration and the applied strain. The net gain for GeSn 13%, $\varepsilon = 2.4\%$ is not calculated since the material is predicted to become a semimetal.

	(100) biaxial tensile strain, $T = 298$ K						
	$\varepsilon = 0\%$	0.4%	0.8%	1.2%	1.6%	2.0%	2.4%
6% Sn	–	–	–	–	1930	5226	7159
					(1×10^{19})	(3×10^{19})	(3×10^{19})
10% Sn	–	–	46	2736	5514	6922	7330
			(5×10^{18})	(3×10^{19})	(3×10^{19})	(3×10^{19})	(3×10^{19})
13% Sn	93	517	2900	5050	6406	7368	
	(1×10^{19})	(1×10^{19})	(3×10^{19})	(3×10^{19})	(3×10^{19})	(3×10^{19})	

in a maximum value of 1848 cm^{-1} at 298 K. The trend is stronger for GeSn with higher Sn concentrations (18% to 22%), with maximum net gains of 3018 cm^{-1}, 3588 cm^{-1}, and 3842 cm^{-1}, respectively [Fig. 6(c)].

As the temperature increases from 25 to 298 K, the net gain decreases in most cases (except for GeSn 22% with the maximum of net gain plateaus between 25 and 150 K). Mechanisms behind that decrease could be different depending on the Sn content. Let us consider GeSn 13%: IVBA, interband, and net absorption spectra of GeSn 13% at 25 K, 150 and 298 K are plotted in Fig. 7(a) for $n_{inj} = 1 \times 10^{19}$ cm^{-3}. At 25 K, the net gain peaks at 0.56 eV; we then track the evolution of IVBA, interband, and net absorption at this energy at 150 and 298 K. While the interband gain decreases significantly, with a loss of 3159 cm^{-1} from 25 to 298 K, IVBA decreases more slowly (with a loss of 395 cm^{-1} over the same temperatures). The net gain decreases rapidly and turns into a net absorption at 298 K. Meanwhile, for higher

Sn concentrations, the impact of interband gain becomes more important. For GeSn 22% and $n_{inj} = 3 \times 10^{19}$ cm^{-3} [Fig. 7(b)], the net gain peaks at 0.40 eV, where IVBA is very weak compared to the interband gain, and remains stable regardless of the temperature. In this case, the variation of the maximum of net gain is mainly driven by interband gain variations.

B. Strained GeSn

We then calculate the net absorption for [100] uniaxial and (100) biaxial tensile-strained GeSn. As mentioned in Sec. II D, we run, for both cases, simulations with light polarized perpendicularly to the direction of applied strain. Due to the large number of possible configuration, we will discuss here only results for tensile-strained GeSn 6%, 10%, 13% at 298 K, with the same values of n_{inj} used in Sec. III A for relaxed GeSn. The maxima of band-to-band net gain are listed in
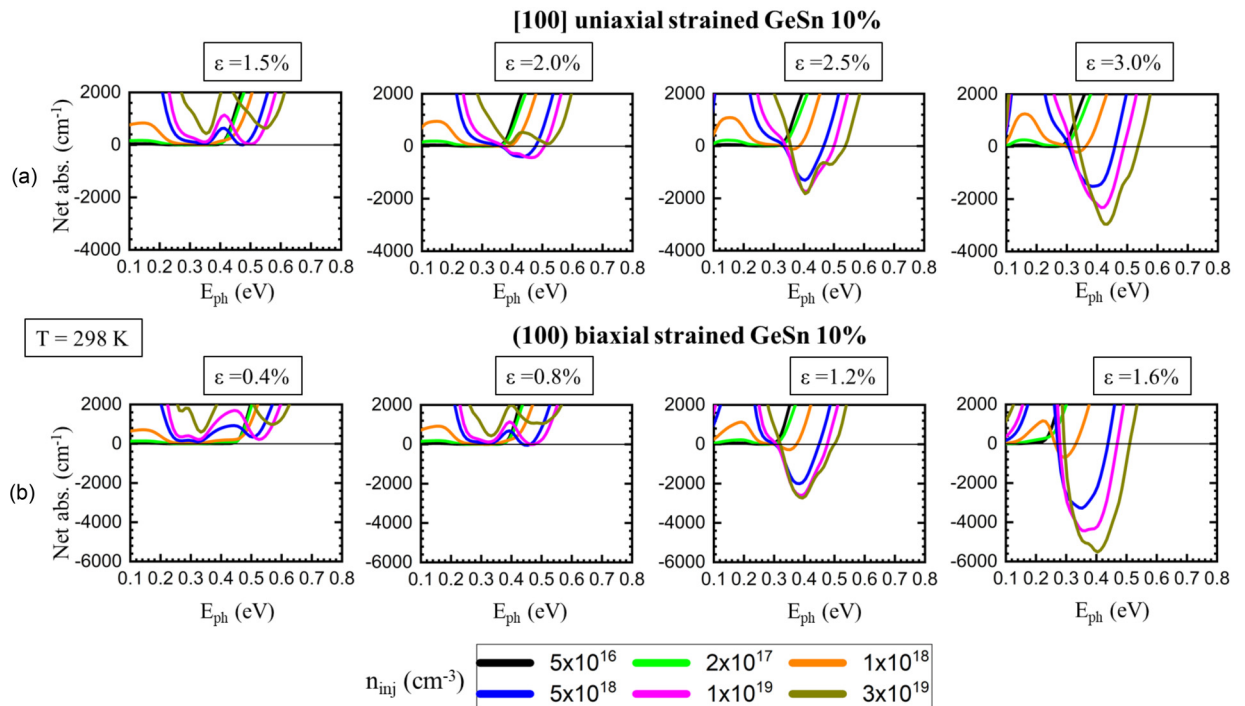

FIG. 8. Net absorption spectra at 298 K, for different strain values (a) of [100] uniaxial strained GeSn 10% and (b) of (100) biaxial strained GeSn 10%.
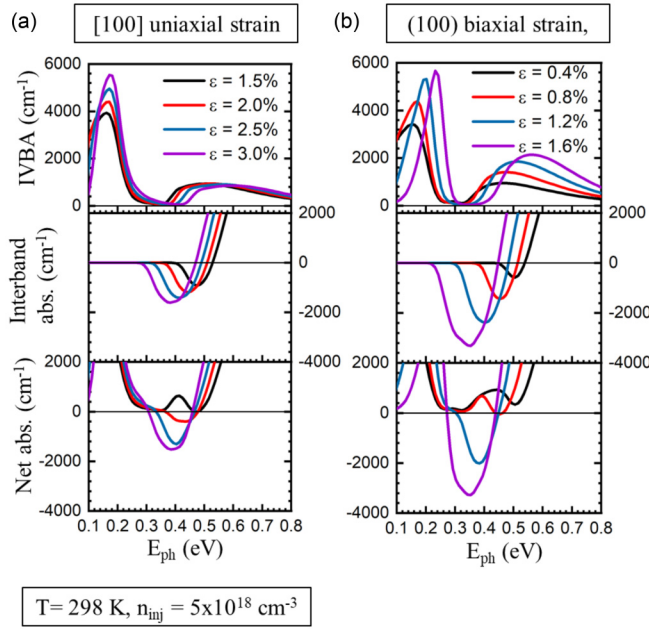
FIG. 9. IVBA, interband, and net absorption spectra at 298 K, $n_{inj} = 5 \times 10^{18}$ cm^{-3} for different strain values of (a) [100] uniaxial strained GeSn 10% and (b) (100) biaxial strained GeSn 10%.

Table VI for [100] uniaxial tensile strain and in Table VII for (100) biaxial tensile strain. We plot in Fig. 8, as an example, the net absorption spectra at different strain values for [100] uniaxial and (100) biaxial strained GeSn 10%.

For both types of tensile strain, the net gain at 298 K starts appearing at lower strain values as the Sn concentration increases. We explain this phenomenon using the same mechanism as for relaxed GeSn (Fig. 9). First, the interband gain increases when the strain increases, thanks to a larger value of $E_{c\Gamma} - E_{cL}$. Then, the overlap between the interband gain and IVBA becomes weaker since the direct gap $E_{g\Gamma}$ decreases and the spin-orbit gap E_{SO} increases at the same time. Here, $E_{g\Gamma} = E_{c\Gamma} - E_{v\text{HH}}$, $E_{SO} = E_{v\text{HH}} - E_{v\text{SO}}$ for [100] uniaxial tensile strained GeSn, and $E_{g\Gamma} = E_{c\Gamma} - E_{v\text{LH}}$, $E_{SO} = E_{v\text{LH}} - E_{v\text{SO}}$ for (100) biaxial tensile strained GeSn. In the [100] uniaxial case, the strong IVBA comes from LH-HH and SO-HH branches, while in the (100) biaxial case, it comes from HH-LH and SO-LH branches.

C. Discussion

From those results, GeSn with high Sn concentrations and/or high applied tensile strains are favorable solutions to make net gain appear at high temperature, eventually at room temperature. The physics behind both approaches are similar to each other, relying simultaneously on an increase of the interband gain and on a decrease of the overlap between the interband gain and IVBA to maximize the net gain. This remark resonates with the theoretical work in Ref. [22], in which the authors presented a similar mechanism guiding the evolution of the net gain of strained Ge as a function of the applied strain. It also agrees qualitatively with the experimental works on GeSn lasers. For relaxed GeSn or GeSn with a slight residual (100) biaxial compressive strain, the maximal laser

temperature was of 80 K for GeSn 8.5% microdisk [2], between 90 and 130 K for GeSn 10.9%–13.3% [2,3,12], between 180 and 230 K for GeSn 16%–17.5% [4,8,11,13], and 270 K for GeSn 20% [10]. In the last case, it should be highlighted that the Sn concentration of 20% was obtained close to the surface of GeSn layer. The actual Sn concentration in the bulk varied gradually, with a mean value estimated around 17.5%–18%. For strained GeSn, Chretien *et al.* showed a record lasing temperature of 273 K, for [100] uniaxial strained GeSn 16% microbridges, with the highest tensile strain around 2.2% at low temperature (25 K) [17]. However, they also reported a decrease of tensile strain as the temperature increased due to the thermal dilatation of the Ge tensor arm.

If we take the presence of net gain as an indication that lasing should occur at a given temperature, simulation overestimates the maximum GeSn lasing temperature. For example, it predicts the existence of net gain in relaxed GeSn at room temperature, for 13% onwards, reaching very high values for GeSn 16%–22%. This is clearly not in line with experimental results. The same remark could be made for strained GeSn, where the net gain reaches colossal values with high applied strain (based on simulations, 4273 cm^{-1} for 3% [100] uniaxial strained GeSn 13%, and 7368 cm^{-1} for 2% [100] biaxial strained GeSn 13%). However, it should be noted that until now we discussed only the band-to-band net gain of GeSn. It is well known that FCA should be considered and added to the band-to-band net gain to correct its value. From the experimental point of view, the heating of the suspended micro-cavity under strong pulsed laser excitation can kick in and introduce a mismatch between the temperature measured in the cryostat (which host the GeSn sample) and the true temperature of the GeSn sample. Cavity loss should also be considered since it sets the minimum net gain required for lasing.

IV. FREE CARRIER ABSORPTION IN GESN

A. Models

The FCA term is now added to the calculation of net absorption. To calculate FCA in a semiconductor material, two approaches are often used.

(1) The Drude-Lorentz's model, which treats the excited charged carriers in semiconductor like an electron gas. The formula of FCA with the Drude-Lorentz's model is as follows [36]:

$$\alpha(\hbar\omega) = \frac{e^3}{\varepsilon_0 c n_r \omega^2} \left(\frac{n_\Gamma}{m_{e\Gamma}^{*2} \mu_{e\Gamma}} + \frac{n_L}{m_{eL}^{*2} \mu_{eL}} \right.$$
$$\left. + \frac{p_{\text{HH}}}{m_{h\text{HH}}^{*2} \mu_{h\text{HH}}} + \frac{p_{\text{LH}}}{m_{h\text{LH}}^{*2} \mu_{h\text{LH}}} \right) \quad (14)$$

with n_Γ, n_L, p_{HH}, p_{LH} are the electron densities in the Γ and L conduction bands, the hole densities in the heavy hole (HH) and light hole (LH) valence bands of Γ, respectively. m^* and μ are the effective mass and the mobility of electrons in Γ, L conduction bands, and of holes in HH, LH valence bands.

(2) The empirical model, which is parametrized from experimental absorption spectrum. It usually takes the form of

$$\alpha(\lambda) = An\lambda^\alpha + Bp\lambda^\beta \quad (15)$$

TABLE VIII. Net gain maximum (in cm^{-1}) with the corresponding value of n_{inj} (in parentheses, in cm^{-3}) for relaxed GeSn, using the Drude-Lorentz's model to calculate FCA.

	25 K	100 K	150 K	220 K	298 K
6% Sn	49 (1×10^{19})	–	–	–	–
10% Sn	2500 (1×10^{19})	1629 (1×10^{19})	932 (1×10^{19})	91 (1×10^{19})	–
13% Sn	2733 (5×10^{18})	1525 (5×10^{18})	846 (1×10^{19})	212 (1×10^{19})	–
16% Sn	2277 (5×10^{18})	1118 (5×10^{18})	600 (1×10^{19})	367 (1×10^{19})	85 (1×10^{19})
18% Sn	1683 (5×10^{18})	1054 (1×10^{19})	855 (1×10^{19})	473 (1×10^{19})	132 (3×10^{19})
20% Sn	1472 (5×10^{18})	869 (1×10^{19})	465 (1×10^{19})	–	–
22% Sn	477 (5×10^{18})	–	–	–	–

with λ being the photon wavelength, n, p the total electron and hole densities, A, B, α, β are constants to be fitted. Similarly to Ref. [22], we assume that the empirical model remains constant regardless of the Sn concentration and the applied strain.

Here, we test the integration of both models in the calculation of net gain for relaxed, undoped GeSn. For the Drude-Lorentz's model, n_Γ, n_L, p_{HH}, p_{LH} and the effective masses are extracted from the EPM band structure. For carriers density in the Γ valley, we calculate n_Γ, p_{HH}, p_{LH} by applying the integrals 6 and 7 on a sphere of wave vectors $\boldsymbol{k}$, centered at Γ point, with $|\boldsymbol{k}| \leqslant 0.075|\boldsymbol{g}|$, where $\boldsymbol{g}$ is one of the basis vectors in the reciprocal space. Assuming electrons in the conduction band are only distributed in the Γ valley and in the L valley, n_L is then: $n_L = n_{\text{inj}} - n_\Gamma$.

In relaxed GeSn, only $m^*_{e\Gamma}$ is isotropic; therefore, approximations should be made for m^*_{eL}, $m^*_{h\text{HH}}$, $m^*_{h\text{LH}}$ because the Drude-Lorentz's model ignores the effective mass anisotropy. For the conduction band in the L valley, the conductivity effective mass is used [37]

$$\frac{1}{m^*_{eL}} = \frac{1}{3}\left(\frac{1}{m^l_{eL}} + \frac{2}{m^t_{eL}}\right). \tag{16}$$

For both the HH and LH valence band, the constant-energy surfaces take a much complex form of a deformed sphere. Here, we calculate their average effective mass $m^*_{h\text{HH}}$ and $m^*_{h\text{LH}}$ using the harmonic mean over all directions in the reciprocal space (the unity sphere of the reciprocal space is discretized into N different directions $\boldsymbol{n}$)

$$\frac{1}{m^*_{h\text{HH}}} = \frac{1}{N}\sum_{\boldsymbol{n}} \frac{1}{m^{\boldsymbol{n}}_{h\text{HH}}}, \tag{17}$$

$$\frac{1}{m^*_{h\text{LH}}} = \frac{1}{N}\sum_{\boldsymbol{n}} \frac{1}{m^{\boldsymbol{n}}_{h\text{LH}}}. \tag{18}$$

In strained GeSn, the situation becomes more complicated due to the anisotropy of $m^*_{e\Gamma}$ and to the difficulty of having a proper definition for heavy holes and light holes. Details and results of the Drude-Lorentz's model in the case of strained GeSn can be found in the Appendix.

Due to the scarcity of experimental data for GeSn carrier mobilities, especially at high Sn concentration, we use an experimental value measured for electrons in n-doped Ge [38,39]: $\mu_{e-n\text{Ge}} = 470 \, \text{cm}^2 \, \text{V}^{-1} \, \text{s}^{-1}$ and suppose that $\mu_{e\Gamma} = \mu_{eL} = \mu_{h\text{HH}} = \mu_{h\text{HH}} = \mu_{e-n\text{Ge}}$. This choice is comparable to the experimental electron and hole mobilities reported for GeSn in Ref. [40] ($\mu_h = 509 \, \text{cm}^2 \, \text{V}^{-1} \, \text{s}^{-1}$ for GeSn 10%), in Ref. [41] ($\mu_h = 428 \, \text{cm}^2 \, \text{V}^{-1} \, \text{s}^{-1}$ for GeSn 9%) and in Ref. [42] ($\mu_e = 440 \, \text{cm}^2 \, \text{V}^{-1} \, \text{s}^{-1}$ for GeSn 4.5%). One might argue that it is still a rather simplistic approximation for the carrier mobilities since they should depend on numerous factors, for example, on the Sn concentration and the injected carrier density. However, we proceed with this assumption to build a starting model of FCA in GeSn, which can be further refined with the expansion of GeSn carrier mobility database.

For the empirical model of FCA, we use the model of Liu *et al.* for Ge [43], once again due to the lack of experimental data for the GeSn absorption spectrum. In both cases (Drude-Lorentz's model and Liu's empirical model), we hypothesize that for a Sn concentration between 6% and 22%, some physical properties of GeSn, here, the absorption spectrum and the carrier mobility, can be approximated reasonably using data from pure Ge.

B. Results and discussion

We calculate the net absorption using the Drude-Lorentz's model and the Liu's empirical model for FCA, under similar conditions of n_{inj}, Sn concentrations, and temperatures of Sec. III A. The maximum of the net gain is shown in Table VIII using the Drude-Lorentz's model for FCA, and in Table IX using Liu's empirical model. There is a clear difference of the impact of these two FCA models on the net gain: compared to the band-to-band calculation, Liu's empirical model reproduces the evolution trend of the maximum of net gain, while the Drude-Lorentz's model predicts that the net gain vanishes at very high Sn concentrations (20% and 22%). While Liu's empirical model has a stronger impact than the Drude-Lorentz's model at low Sn concentrations between 6%

TABLE IX. Net gain maximum (in cm^{-1}) with the corresponded value of n_{inj} (in parentheses, in cm^{-3}) for relaxed GeSn, using the Liu's empirical model to calculate FCA.

	25 K	100 K	150 K	220 K	298 K
6% Sn	−	−	−	−	−
10% Sn	2282	1350	630	−	−
	(5×10^{18})	(5×10^{18})	(1×10^{19})		
13% Sn	2721	1496	767	39	−
	(5×10^{18})	(5×10^{18})	(5×10^{18})	(5×10^{18})	
16% Sn	2583	1406	814	425	50
	(5×10^{18})	(5×10^{18})	(5×10^{18})	(5×10^{18})	(5×10^{18})
18% Sn	2445	1857	1502	1033	456
	(5×10^{18})	(5×10^{18})	(1×10^{19})	(1×10^{19})	(1×10^{19})
20% Sn	3369	2539	2109	1404	589
	(5×10^{18})	(1×10^{19})	(1×10^{19})	(1×10^{19})	(1×10^{19})
22% Sn	3916	3005	2359	1391	426
	(5×10^{18})	(1×10^{19})	(1×10^{19})	(1×10^{19})	(1×10^{19})

and 13%, with lower maximum of net gain, the situation is inverted for high Sn concentrations between 16% and 22%.

We plot in Fig. 10 FCA spectra at 298 K, at $n_{\mathrm{inj}} = 5 \times 10^{18}$ cm^{-3} and 1×10^{19} cm^{-3}, for Liu's empirical model and the Drude-Lorentz's model for Sn concentrations between 10% and 22%. While Liu's empirical model is independent of the Sn concentration, the Drude-Lorentz's model depends strongly on this variable: For GeSn 10% and 13%, the latter yields lower FCA than the former. These two models yield
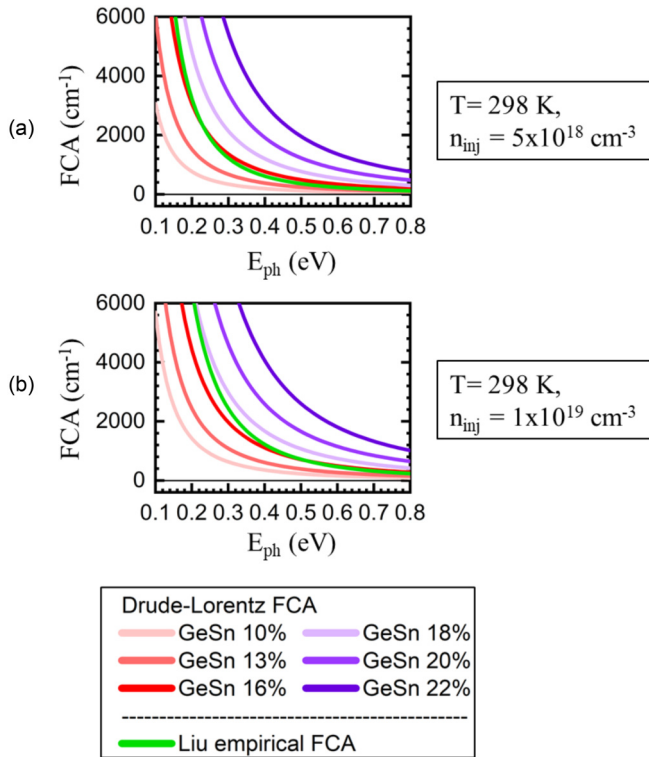

FIG. 10. Comparison between the Drude-Lorentz's model and Liu's empirical model of FCA, for relaxed GeSn with a Sn concentration between 10% and 22% at (a) $n_{\mathrm{inj}} = 5 \times 10^{18}$ cm^{-3} and (b) $n_{\mathrm{inj}} = 1 \times 10^{19}$ cm^{-3}.

comparable results for GeSn 16%. From GeSn 18% upward, the Drude-Lorentz's model yields higher FCA and eventually it becomes strong enough at GeSn 20%–22% to suppress the net gain.

To explain the evolution of Drude-Lorentz's FCA and the Sn concentration, first we plot the contribution of each type of charged carrier (Γ electrons, L electrons, light holes, and heavy holes) in the total FCA [Fig. 11(a)]: The contribution of Γ electrons increases with the Sn concentration, and eventually becomes the dominant factor at very high Sn concentration (between 16% and 22% Sn). Since these contributions are proportional to the terms $\frac{n}{m_e^{*2} \mu_e}$ and $\frac{p}{m_h^{*2} \mu_h}$ in Eq. (14), we should look at the carrier density and the effective mass in each term.

For electrons, when the Sn concentration increases, $E_{c\Gamma} - E_{cL}$ becomes more negative: More electrons is thus located in the Γ valley [Fig. 11(b)]. At the same time, $m_{e\Gamma}^*$ decreases, while m_{eL}^* keeps the same value regardless of the Sn concentration [Fig. 11(c)]. The decrease of $m_{e\Gamma}^*$ observed in this work and in other calculation [1,29,44] can be explained using the perturbation theory [28], showing a smaller effective mass when the direct gap shrinks. Therefore, the FCA contribution from Γ electrons increases with the Sn concentration, while the FCA contribution from L electrons decreases. The simultaneous effect of an increased value of n_Γ and a decreased value of $m_{e\Gamma}^*$ makes the gain of FCA from Γ electrons outweigh the loss from L electrons, which leads to an increase of the full FCA with the Sn concentration, as seen in Fig. 10.

For holes, while the light hole effective mass $m_{h\mathrm{LH}}^*$ is comparable to $m_{e\Gamma}^*$ [Fig. 11(c)], most of the holes are located in the heavy hole band due to its higher density of states (i.e., higher effective mass) and to the relative position between these two valence bands, with a degeneracy at the Γ point. The FCA contribution from both types of holes is therefore much weaker than that of Γ electrons. Combined with the previous remark on the FCA contribution of Γ electrons and L electrons, it explains why, in the Drude-Lorentz's model, the main FCA contribution comes from Γ electrons at very high Sn concentration.
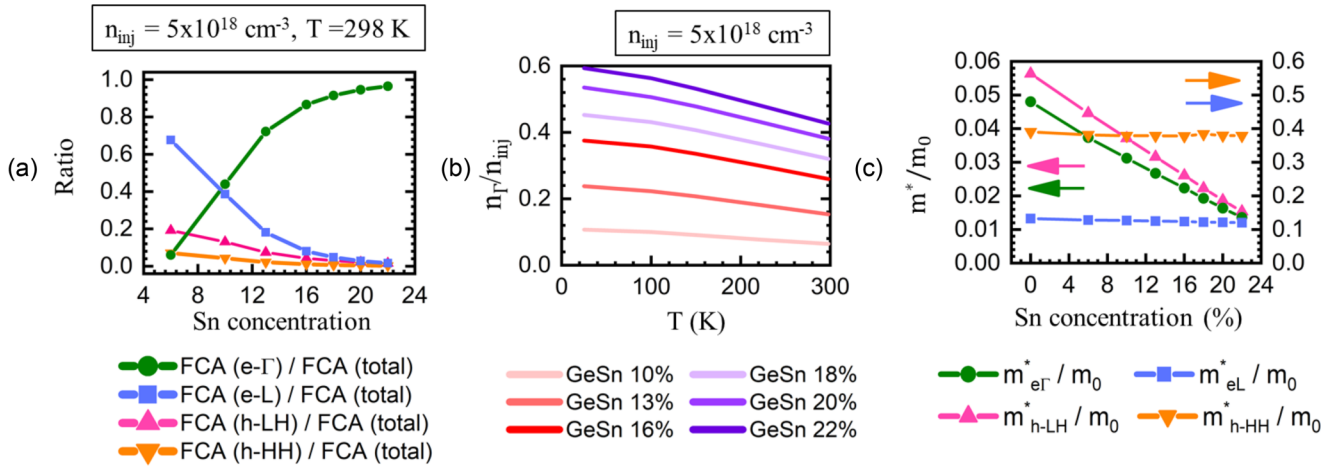
FIG. 11. (a) The contribution of each term in the total Drude-Lorentz FCA at 298 K: electrons in the Γ and L conduction bands ($e - \Gamma$, $e - L$), light holes ($h - $LH) and heavy holes ($h - $HH), $n_{\text{inj}} = 5 \times 10^{18}$ cm^{-3}. The total FCA is normalized to 1. (b) The ratio $\frac{n_\Gamma}{n_{\text{inj}}}$ at $n_{\text{inj}} = 5 \times 10^{18}$ cm^{-3} for relaxed GeSn with Sn between 10% and 22%, as a function of the temperature. (c) The ratio $\frac{m^*}{m_0}$ for $e - \Gamma$, $e - L$, $h - $LH and $h - $HH as a function of the Sn concentration. The arrows indicate the corresponding y-axis in each case.

On the other side, since both models show that FCA $\propto \lambda^k$, with $k \geqslant 2$, when the interband gain shifts towards lower photon energy as the direct gap shrinks, the contribution of FCA on the net gain becomes more important. The calculation of total net gain for relaxed GeSn, especially at high Sn concentration, depends strongly on the choice of FCA model. The same remark can be made for high [100] uniaxial-(100) biaxial tensile strained GeSn. Therefore, measurements of absorption spectrum, especially for GeSn with small direct gap, should be conducted to gain further insight on the FCA. Right now, these tasks remain a challenge from an experimental point of view, stemming from the fragility of highly strained GeSn structure [17] and from the gradual distribution of Sn atoms in high Sn content GeSn layers [10,45]. A more in-depth theoretical calculation of FCA is also necessary, to take into account phonon-assisted, charge impurity-assisted intravalley and intervalley transitions, as presented in Refs. [18,46].

V. LASING CHARACTERISTICS OF GeSn OPTICAL CAVITY

With the calculated net gain, we use the formalism of Sec. II E to study the lasing characteristics of GeSn optical cavities. We limit the calculation to two cases. First, we study relaxed GeSn 16%, where the maximal lasing temperature is reported to be 230 K [13]. Then, we study GeSn 6% with 1.27% of (100) biaxial tensile strain. Continuous wave (i.e., with a very low threshold) lasing was demonstrated experimentally in GeSn with a Sn concentration close to that (5.4%), with 1.27% and 1.4% of (100) biaxial strain [14,15]. The mode position and the optical confinement were taken from experimental data. The choices of various parameters (C_{sp}, E_{pump}, α_{pump}, β_{rad}, C_n, C_p, Γ_p) and the depths of the experimental GeSn gain medium are shown in Table X. Here, for GeSn, we choose a radiative recombination coefficient value β_{rad} comparable to other direct-gap semiconductor, between

1×10^{-11} cm^3 s-1 and 1×10^{-8} cm^3 s-1, as reported in Ref. [47]. Due to questions remaining on the choice of FCA model—as shown in Sec. IV—unless there is notification, all lasing characteristics are calculated using the band-to-band net gain.

We plot in Fig. 12(a) the simulated lasing characteristics, linking the emitted photon density S_p to the pump power P, for relaxed GeSn 16% at 15 K with two quality factors: $Q = 200$ and $Q = 2000$, corresponding, respectively, to $\alpha_{\text{cav}} = 473.5$ cm^{-1} and $\alpha_{\text{cav}} = 47.3$ cm^{-1}. Due to the lack of experimental data for τ_{nrad} in GeSn 16%, τ_{nrad} is set here at 170 ps—the experimental value reported for GeSn 12.5%, extracted from pump-probe measurement [19]. Despite a 10-fold difference concerning cavity loss, the simulated lasing threshold P_{th} stabilizes and varies only between 43 kW cm^{-2} and 36 kW cm^{-2}. It is explained by looking at the variation of net absorption as a function of n_{inj}, at the laser mode position [Fig. 12(b)]: The net gain starts appearing at $n_{\text{inj}} = 3.5 \times 10^{17}$ cm^{-3} and increases rapidly with n_{inj} up to 1×10^{18} cm^{-3}. Therefore, the threshold densities (i.e., the injected carrier density required to reach the threshold gain $g = \frac{\alpha_{\text{cav}}}{\Gamma_p}$) for $Q = 200$ and $Q = 2000$ are very close, respectively, at

TABLE X. Parameters used for laser equations.

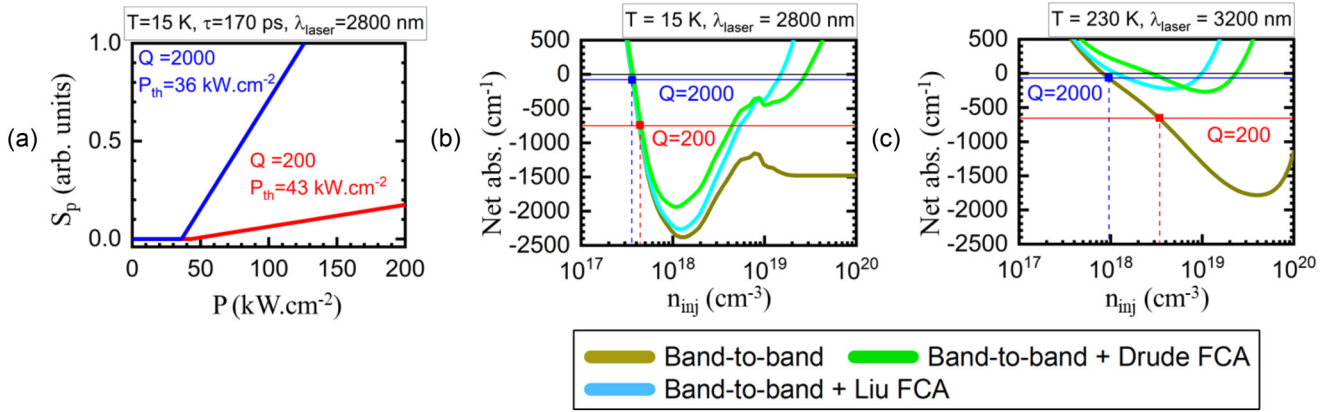| Parameter	Value
C_{sp}	0.01
E_{pump}(eV)	1.1676 [13,14]
α (cm^{-1})	21550 [48]
β_{rad} (cm^3 s^{-1})	1×10^{-10}
C_n, C_p (cm^6 s^{-1})	5×10^{-31} [19]
d_0, d_1 (nm)	115, 533 (GeSn 16%) [13]
	0, 300 (GeSn 6%) [14]
Γ_p	0.634 (GeSn 16%)
	0.842 (GeSn 6%)

FIG. 12. (a) Lasing characteristics of a relaxed GeSn 16% optical cavity at 15 K, for $Q = 2000$ and $Q = 200$, at lasing wavelength $\lambda_{\text{laser}} = 2800$ nm. (b, c) Net absorption as a function of n_{inj} at 15 K ($\lambda_{\text{laser}} = 2800$ nm) and at 230 K ($\lambda_{\text{laser}} = 3200$ nm), calculated for three different models: band-to-band (without FCA), band-to-band with Drude-Lorentz FCA, and band-to-band with Liu's empirical FCA. The blue and red straight lines indicate the threshold gain $g = \frac{\alpha_{\text{cav}}}{\Gamma_p}$ for $Q = 2000$ and for $Q = 200$.

4.4×10^{17} cm^{-3} and 3.7×10^{17} cm^{-3}. Here, changing the quality factor of the optical cavity has some limited impact on the lasing threshold. It should also be noted that for relaxed GeSn 16% at 15 K, FCA is very small due to the low threshold density around 10^{17} cm^{-3}: Different models of GeSn net gain (band-to-band calculation, with or without FCA) give similar results in this case.

When the temperature increases, the effect of the cavity loss becomes more important [Fig. 12(c)]: At 230 K, due to a shift of lasing mode toward higher wavelengths observed in the experiments, $Q = 200$ and $Q = 2000$ corresponds to $\alpha_{\text{cav}} = 414.3$ cm^{-1} and $\alpha_{\text{cav}} = 41.4$ cm^{-1}. Here, the net gain increases more slowly with n_{inj}. Therefore, the threshold densities for two values of Q differ significantly, at 3.4×10^{18} cm^{-3} and 9.5×10^{17} cm^{-3}. The FCA contribution also becomes important in this range of n_{inj}: The threshold density at $Q = 2000$ depends now on the choice of net gain model, with or without FCA. Here, FCA strongly reduces the net gain and makes a GeSn optical cavity with high loss ($Q = 200$) unfit for lasing.

Next, we plot in Fig. 13(a) the lasing characteristics of relaxed GeSn 16% at 15 K, with $Q = 2000$ and τ_{nrad} varying between 17 and 1700 ps. Indeed, a higher value of τ_{nrad}—representing a GeSn layer with a better crystalline quality, less trap defects and dislocations—leads to a smaller lasing threshold. Below and near the lasing threshold, with low value of n_{inj} (inferior to 3.7×10^{17} cm^{-3}), the Shockley-Read-Hall nonradiative recombination is the main recombination mechanism. Therefore, the carrier continuity Eq. (8) can be approximated as

$$\frac{P(e^{-\alpha d_0} - e^{-\alpha d_1})}{E_{\text{pump}}(d_1 - d_0)} \approx \frac{n}{\tau_{\text{nrad}}}, \quad (19)$$

which leads to

$$P \approx \frac{E_{\text{pump}}(d_1 - d_0)}{(e^{-\alpha d_0} - e^{-\alpha d_1})} \frac{n}{\tau_{\text{nrad}}}, \quad (20)$$

hence the inverse proportionality between P_{th} and τ_{nrad} shown in Fig. 13(a).

At low temperature, the results suggest that the crystalline quality of GeSn is the most important factor controlling the lasing threshold. To check this remark, we plot in Fig. 13(b) the lasing characteristics of relaxed GeSn 16% ($E_{c\Gamma} - E_{\text{cL}} = -0.157$ eV) and 1.27% (100) biaxial tensile-strained GeSn 6% ($E_{c\Gamma} - E_{\text{cL}} = -0.083$ eV), using the same values of Q and τ_{nrad}. Despite the difference of $E_{c\Gamma} - E_{\text{cL}}$, plus the lasing mode position, P_{th} are quite similar, at 3.7 kW cm^{-2} and 2.9 kW cm^{-2}, respectively. The lasing threshold of GeSn 16%
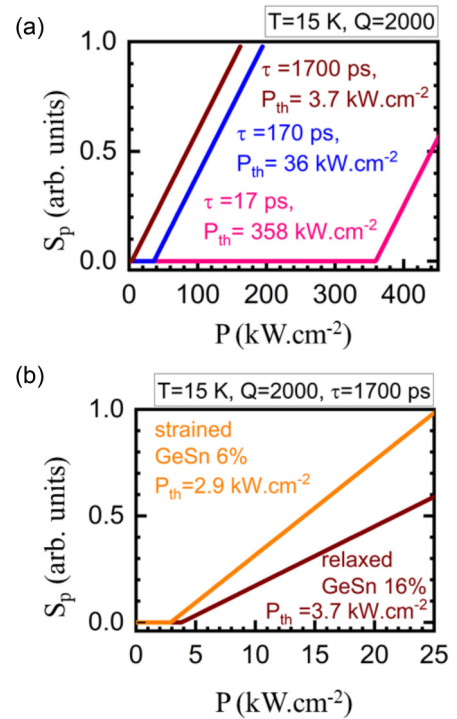

FIG. 13. (a) Lasing characteristics of relaxed GeSn 16% optical cavity at 15 K, for $\tau_{\text{nrad}} = 1700$ ps, 170 ps, and 17 ps at lasing wavelength $\lambda_{\text{laser}} = 2800$ nm. (b) Lasing characteristics of relaxed GeSn 16% optical cavity ($\lambda_{\text{laser}} = 2800$ nm) and 1.27% (100) biaxial strained GeSn 6% ($\lambda_{\text{laser}} = 2350$ nm) at 15 K.

is slightly higher, in part due to a lower value of $\frac{(e^{-\alpha d_0} - e^{-\alpha d_1})}{(d_1 - d_0)}$ (i.e., less lights are absorbed). The experimental results show, however, a contrast: with the same type of optical cavity (microdisk), relaxed GeSn 16% gives $P_{th} = 134\,\text{kW\,cm}^{-2}$ at 15 K, while 1.27% (100) biaxial tensile strained GeSn 5.4% gives $P_{th} = 5\,\text{kW\,cm}^{-2}$.

Using Eq. (20) and the experimental value of P_{th}, we estimate $\tau_{\text{nrad}} = 47\,\text{ps}$ for relaxed GeSn 16% and $\tau_{\text{nrad}} = 986\,\text{ps}$ for strained GeSn 6%. For GeSn 16%, this value is lower than the GeSn 12.5% experimental value [19], suggesting a lower crystal quality. It can be explained by a higher lattice parameter mismatch between the GeSn layer and the Ge buffer during the epitaxial growth which is performed at a lower temperature, favoring the presence of dislocation and defect in the material [49,50]. For GeSn 6%, this value is higher than the GeSn 12.5% experimental value. It can be attributed to more favorable conditions for epitaxy, with a lower lattice parameter mismatch with the Ge buffer and a higher epitaxy temperature, resulting in a better crystalline quality. Compared to the lifetimes published by De Cesari *et al.* [51] (τ_{nrad} estimated between 1500 and 2300 ps for GeSn 5% at 7 K) and Elbaz *et al.* [15] (τ_{nrad} estimated between 1400 ps and 2100 ps for GeSn 5.4% at 25 K), the estimated value of τ_{nrad} for GeSn 6% is lower. Surface reflectivity—which is not considered in this work—might explain those differences.

As discussed in Sec. III C, GeSn with high Sn concentration and/or with high [100] uniaxial-(100) biaxial tensile strains are solutions to achieve GeSn lasing at room temperature. In addition, from the simulation of GeSn lasing characteristics, a high crystalline quality—and therefore a high value of τ_{nrad}—is critical to reduce lasing threshold at low temperature. This remark remains valid at higher temperature, even when the effect of cavity loss becomes more significant. Therefore, to obtain a GeSn laser with low lasing threshold at room temperature, one might target GeSn with low or medium Sn concentrations together with a very high tensile strain.

Such an approach yields net optical gain at room temperature, and is more likely to result in high crystalline quality GeSn under the constraints of current epitaxy technology. Better crystalline quality also enables GeSn to withstand higher mechanical stress and prevents the material from fracturing under high tensile strains.

VI. CONCLUSION

We calculated the band-to-band net gain of relaxed and strained GeSn. We showed that it was determined not only by the amplitude of interband gain, controlled by the difference between the conduction band energies at Γ and L valley, but also by the relative position between the interband gain and the intervalence band absorption, controlled by the difference between the direct gap and the spin-orbit gap. Both approaches, GeSn with high Sn concentration and/or with high [100] uniaxial-(100) biaxial tensile strain can make the net gain appear at higher temperature and eventually at room temperature. We then discussed the integration of free carrier absorption into the calculation of net gain and showed that different models give contrasted results, especially for GeSn with a small direct band gap. Experimental measurements of absorption spectrum and in-depth theoretical calculation are thus needed to gain further insight on this topic. Finally, we simulated the lasing characteristics for relaxed GeSn 16% and (100) biaxial tensile-strained GeSn 6% optical cavities. We found that both the cavity loss and crystalline quality—with the later having a direct impact on the nonradiative lifetime—altered the lasing threshold, but in different ways: while crystalline quality had a strong impact on the lasing threshold regardless of the temperature, cavity loss had very limited impact at low temperature and became more significant as the temperature increased. Given those results, we suggest using low/medium Sn concentration GeSn under very high [100] uniaxial or (100) biaxial tensile strain to obtain low threshold lasing at room temperature.
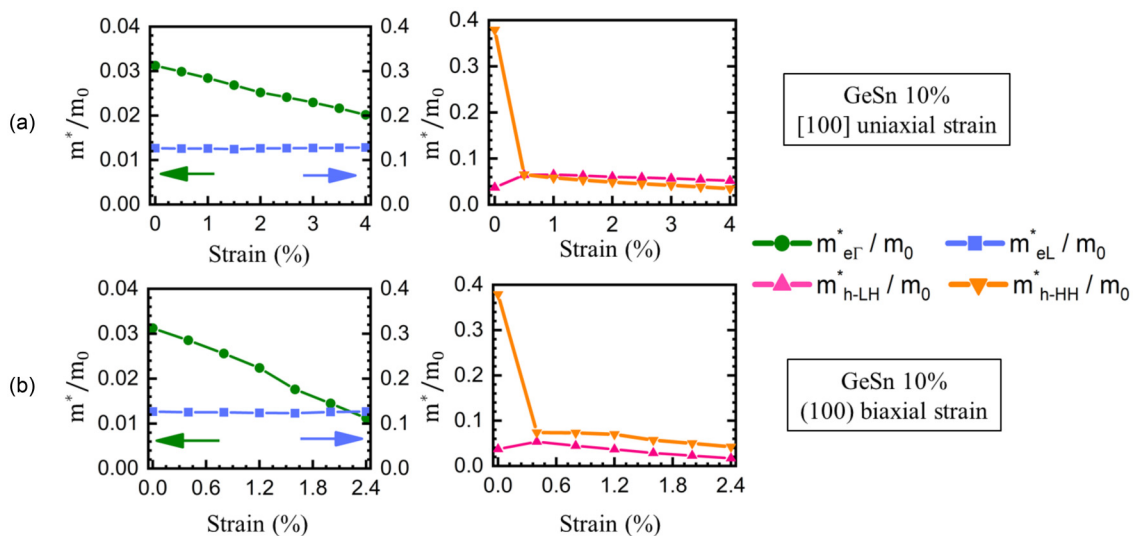

FIG. 14. (a) Evolution of $m_{e\Gamma}^*$, m_{eL}^*, $m_{h-\text{LH}}^*$, and $m_{h-\text{HH}}^*$ as functions of the applied strain, for (a) GeSn 10% under [100] uniaxial tensile strain and (b) GeSn 10% under [100] biaxial tensile strain.

TABLE XI. Net gain maximum (in cm^{-1}) with the corresponding value of n_{inj} (in parenthesis, in cm^{-3}) at 298 K in [100] uniaxial tensile-strained GeSn, with n_{inj} between 5×10^{16} cm^{-3} and 3×10^{19} cm^{-3}, extracted for Drude-Lorentz's model and Liu's empirical model of FCA.

	[100] uniaxial tensile strain-Drude-Lorentz FCA								
	$\varepsilon = 0\%$	0.5%	1.0%	1.5%	2.0%	2.5%	3.0%	3.5%	4.0%
6% Sn	–	–	–	–	–	–	–	986 (1×10^{19})	1827 (3×10^{19})
10% Sn	–	–	–	–	28 (5×10^{18})	976 (1×10^{19})	1484 (3×10^{19})	2211 (3×10^{19})	1972 (3×10^{19})
13% Sn	–	–	–	313 (1×10^{19})	841 (1×10^{19})	1111 (3×10^{19})	1341 (3×10^{19})	728 (3×10^{19})	–
	[100] uniaxial tensile strain-Liu′s empirical FCA								
	$\varepsilon = 0\%$	0.5%	1.0%	1.5%	2.0%	2.5%	3.0%	3.5%	4.0%
6% Sn	–	–	–	–	–	–	–	442 (5×10^{18})	968 (1×10^{19})
10% Sn	–	–	–	–	–	707 (5×10^{18})	1246 (1×10^{19})	1205 (1×10^{19})	1136 (3×10^{19})
13% Sn	–	–	–	389 (5×10^{18})	924 (1×10^{19})	1297 (1×10^{19})	1254 (1×10^{19})	1211 (3×10^{19})	565 (3×10^{19})

APPENDIX: FREE CARRIER ABSORPTION IN STRAINED GeSn

In strained GeSn, $m_{e\Gamma}^*$ becomes anisotropic. Here, we calculate all the effective masses $m_{e\Gamma}^*$, m_{eL}^*, m_{hLH}^*, and m_{hHH}^* using the harmonic mean over all directions in the reciprocal space, similar to the method adopted for m_{hHH}^* and m_{hLH}^* in relaxed GeSn. We plot, in Fig. 14, the values of $m_{e\Gamma}^*$, m_{eL}^*, m_{hLH}^*, and m_{hHH}^* for GeSn 10% under [100] uniaxial and (100) biaxial tensile strain. For the L electrons, the applied strain has very little impact on m_{eL}^*: Its values barely change and they are very similar to the conductivity effective mass calculated in relaxed GeSn.

TABLE XII. Net gain maximum (in cm^{-1}) with the corresponding value of n_{inj} (in parentheses, in cm^{-3}) at 298 K in (100) biaxial tensile-strained GeSn, with n_{inj} between 5×10^{16} cm^{-3} and 3×10^{19} cm^{-3}, extracted for Drude-Lorentz's model and Liu's empirical model of FCA.

	(100) biaxial tensile strain-Drude-Lorentz FCA						
	$\varepsilon = 0\%$	0.4%	0.8%	1.2%	1.6%	2.0%	2.4%
6% Sn	–	–	–	–	1370 (1×10^{19})	3609 (3×10^{19})	4336 (3×10^{19})
10% Sn	–	–	–	1597 (1×10^{19})	2490 (3×10^{19})	2038 (3×10^{19})	–
13% Sn	–	–	926 (1×10^{19})	1564 (1×10^{19})	–	–	
	(100) biaxial tensile strain-Liu′s empirical FCA						
	$\varepsilon = 0\%$	0.4%	0.8%	1.2%	1.6%	2.0%	2.4%
6% Sn	–	–	–	–	1061 (5×10^{18})	3365 (1×10^{19})	3931 (1×10^{19})
10% Sn	–	–	–	1331 (5×10^{18})	3057 (1×10^{19})	3720 (1×10^{19})	3776 (3×10^{19})
13% Sn	–	–	938 (1×10^{19})	2442 (1×10^{19})	3175 (1×10^{19})	3550 (3×10^{19})	

For holes, the situation becomes more complicated. Under both types of strain, m^*_{hHH} drops, becoming comparable to m^*_{hLH}. This phenomenon was already observed by Rainko *et al.* in their work on (100) biaxial strained GeSn [18]. It is thus difficult—based solely on the band energy position—to define properly the terms "heavy holes" and "light holes" for strained GeSn, in contrast to relaxed GeSn. Therefore, here, for [100] uniaxial and (100) biaxial strained GeSn, we calculate the Drude-Lorentz FCA only with the contribution from the Γ electrons and the L electrons, omitting the contribution from holes. On the other side, Liu's empirical model will be used once again to compare with the Drude-Lorentz's model.

We extract, in Tables XI and XII, the maxima of net gain at 298 K for [100] uniaxial strained–(100) biaxial strained GeSn, with contributions from the Drude-Lorentz's model and Liu's empirical model. For [100] uniaxial strain, Liu's empirical model has a stronger impact on the net gain than the Drude-Lorentz's model in every case, except for highly strained GeSn 13%. For (100) biaxial strain, like relaxed GeSn, a clear difference can be seen in small direct gap GeSn (i.e., under high tensile strain): the Drude-Lorentz's model suppresses the net gain at 2.4% strained GeSn 10% and from 1.6% strained GeSn 13%, while Liu's empirical model predicts a strong net gain for these configurations. It is explained by a faster decline of $m^*_{e\Gamma}$ under (100) biaxial strain compared to [100] uniaxial strain, hence a stronger FCA.

[1] S. Wirths, R. Geiger, N. von den Driesch, G. Mussler, T. Stoica, S. Mantl, Z. Ikonic, M. Luysberg, S. Chiussi, J.-M. Hartmann, H. Sigg, J. Faist, D. Buca, and D. Grutzmacher, Nat. Photon. **9**, 88 (2015).

[2] D. Stange, S. Wirths, R. Geiger, C. Schulte-Braucks, B. Marzban, N. von den Driesch, G. Mussler, T. Zabel, T. Stoica, J.-M. Hartmann, S. Mantl, Z. Ikonic, D. Grutzmacher, H. Sigg, J. Witzens, and D. Buca, ACS Photon. **3**, 1279 (2016).

[3] S. Al-Kabi, S. A. Ghetmiri, J. Margetis, T. Pham, Y. Zhou, W. Dou, B. Collier, R. Quinde, W. Du, A. Mosleh, J. Liu, G. Sun, R. A. Soref, J. Tolle, B. Li, M. Mortazavi, H. A. Naseem, and S.-Q. Yu, Appl. Phys. Lett. **109**, 171105 (2016).

[4] V. Reboud, A. Gassenq, N. Pauc, J. Aubin, L. Milord, Q. M. Thai, M. Bertrand, K. Guilloy, D. Rouchon, J. Rothman, T. Zabel, F. T. A. Pilon, H. Sigg, A. Chelnokov, J.-M. Hartmann, and V. Calvo, Appl. Phys. Lett. **111**, 092101 (2017).

[5] S. Bao, D. Kim, C. Onwukaeme, S. Gupta, K. C. Saraswat, K. H. Lee, Y. Kim, D. Min, Y. Jung, H. Qiu, H. Wang, E. A. Fitzgerald, C. S. Tan, and D. Nam, Nat. Commun. **8**, 1845 (2017).

[6] A. Elbaz, M. El-Kurdi, A. Aassime, S. Sauvage, X. Checoury, I. Sagnes, C. Baudot, F. Boeuf, and P. Boucaud, APL Photon. **3**, 106102 (2018).

[7] F. T. A. Pilon, A. Lyasota, Y.-M. Niquet, V. Reboud, V. Calvo, N. Pauc, J. Widiez, C. Bonzon, J.-M. Hartmann, A. Chelnokov, J. Faist, and H. Sigg, Nat. Commun. **10**, 2724 (2019).

[8] J. Margetis, S. Al-Kabi, W. Du, W. Dou, Y. Zhou, T. Pham, P. Grant, S. A. Ghetmiri, A. Mosleh, B. Li, J. Liu, G. Sun, R. A. Soref, J. Tolle, M. Mortazavi, and S.-Q. Yu, ACS Photon. **5**, 827 (2017).

[9] J. Margetis, Y. Zhou, W. Dou, P. Grant, B. Alharthi, W. Du, A. Wadsworth, Q. Guo, H. Tran, S. Ojo, G. Abernathy, A. Mosleh, S. A. Ghetmiri, G. B. Thompson, J. Liu, G. Sun, R. A. Soref, J. Tolle, B. Li, M. Mortazavi, and S.-Q. Yu, Appl. Phys. Lett. **113**, 221104 (2018).

[10] Y. Zhou, W. Dou, W. Du, S. Ojo, H. Tran, S. A. Ghetmiri, J. Liu, G. Sun, R. A. Soref, J. Margetis, J. Tolle, B. Li, Z. Chen, M. Mortazavi, and S.-Q. Yu, ACS Photon. **6**, 1434 (2019).

[11] W. Du, Q. M. Thai, J. Chrétien, M. Bertrand, L. Casiez, Y. Zhou, J. Margetis, N. Pauc, A. Chelnokov, V. Reboud, V. Calvo, J. Tolle, L. Baohua, and S.-Q. Yu, Front. Phys. **7**, 147 (2019).

[12] D. Stange, N. von den Driesch, T. Zabel, F. T. A. Pilon, D. Rainko, B. Marzban, P. Zaumseil, J.-M. Hartmann, Z. Ikonic, G. Capellini, S. Mantl, H. Sigg, J. Witzens, D. Grutzmacher, and D. Buca, ACS Photon. **5**, 4628 (2018).

[13] Q. M. Thai, N. Pauc, J. Aubin, M. Bertrand, J. Chrétien, V. Delaye, A. Chelnokov, J.-M. Hartmann, V. Reboud, and V. Calvo, Opt. Express **26**, 32500 (2018).

[14] A. Elbaz, Thèse: Sources laser compatibles silicium à base de Ge et GeSn à bande interdite directe, Ph.D. thesis, Université Paris-Saclay, 2019, https://tel.archives-ouvertes.fr/tel-02100605.

[15] A. Elbaz, D. Buca, N. von den Driesch, K. Pantzas, G. Patriarche, N. Zerounian, E. Herth, X. Checoury, S. Sauvage, I. Sagnes, A. Foti, R. Ossikovski, J.-M. Hartmann, F. Boeuf, Z. Ikonic, P. Boucaud, D. Grutzmacher, and M. El-Kurdi, Nat. Photon. **14**, 375 (2020).

[16] Q. M. Thai, N. Pauc, J. Aubin, M. Bertrand, J. Chrétien, A. Chelnokov, J.-M. Hartmann, V. Reboud, and V. Calvo, Appl. Phys. Lett. **113**, 051104 (2018).

[17] J. Chrétien, N. Pauc, F. T. A. Pilon, M. Bertrand, Q. M. Thai, L. Casiez, N. Bernier, H. Dansas, P. Gergaud, E. Delamadeleine, R. Khazaka, H. Sigg, J. Faist, A. Chelnokov, V. Reboud, J.-M. Hartmann, and V. Calvo, ACS Photon. **6**, 2462 (2019).

[18] D. Rainko, Z. Ikonic, A. Elbaz, N. von den Driesch, D. Stange, E. Herth, P. Boucaud, M. El-Kurdi, D. Grutzmacher, and D. Buca, Sci. Rep. **9**, 259 (2019).

[19] R. Geiger, Thesis: Direct Band Gap Germanium for Si-compatible Lasing, Ph.D. thesis, ETH Zurich, 2016.

[20] M. J. Suess, R. Geiger, R. A. Minamisawa, G. Schiefler, J. Frigerio, D. Chrastina, G. Isella, R. Spolenak, J. Faist, and H. Sigg, Nat. Photon. **7**, 466 (2013).

[21] L. Carroll, P. Friedli, S. Neuenschwander, H. Sigg, S. Cecchi, F. Isa, D. Chrastina, G. Isella, Y. Fedoryshyn, and J. Faist, Phys. Rev. Lett. **109**, 057402 (2012).

[22] S. Gupta, D. Nam, J. Vuckovic, and K. C. Saraswat, Phys. Rev. B **97**, 155127 (2018).

[23] M. Yamada, *Theory of Semiconductor Lasers: From Basis of Quantum Electronics to Analyses of the Mode Competition Phenomena and Noise* (Springer, New York, 2014).

[24] J. R. Chelikowsky and M. L. Cohen, Phys. Rev. B **14**, 556 (1976).

[25] M. M. Rieger and P. Vogl, Phys. Rev. B **48**, 14276 (1993).

[26] M. Bertrand, Q. M. Thai, J. Chrétien, N. Pauc, J. Aubin, L. Milord, A. Gassenq, J.-M. Hartmann, A. Chelnokov, V. Calvo, and V. Reboud, Ann. Phys. (Leipzig) **531**, 1800396 (2019).

[27] C. G. Van de Walle, Phys. Rev. B **39**, 1871 (1989).

[28] P. Yu and M. Cardona, *Fundamentals of Semiconductors: Physics and Materials Properties* (Springer, New York, 2005).

[29] K. L. Low, Y. Yang, G. Han, W. Fan, and Y.-C. Yeo, J. Appl. Phys. **112**, 103715 (2012).

[30] J. Kim and M. V. Fischetti, J. Appl. Phys. **108**, 013710 (2010).

[31] S. M. Sze and K. N. Kwok, *Physics of Semiconductor Devices* (Wiley, New York, 2006).

[32] Y. P. Varshni, Physica **34**, 149 (1967).

[33] S. L. Chuang, *Physics of Optoelectronic Devices* (Wiley, New York, 1995).

[34] V. Reboud, A. Gassenq, N. Pauc, J. Aubin, Q. M. Thai, M. Bertrand, L. Milord, E. Martinez, C. Licitra, D. Rouchon, J. Rothman, F. T. A. Pilon, T. Zabel, H. Sigg, A. Chelnokov, J.-M. Hartmann, and V. Calvo, in *Proceedings of the 14th International Conference on Group IV Photonics* (IEEE, New York, 2017), p. 13.

[35] H. J. Monkhorst and J. D. Pack, Phys. Rev. B **13**, 5188 (1976).

[36] G.-E. Chang and H. H. Cheng, J. Phys. D **46**, 065103 (2013).

[37] A. H. Kahn, Phys. Rev. **97**, 1647 (1955).

[38] K. Guilloy, Thèse: Germanium déformé pour l'émission de lumière, Ph.D. thesis, Université Grenoble-Alpes, 2016, https://tel.archives-ouvertes.fr/tel-01456920.

[39] C. Hilsum, Electron. Lett. **10**, 259 (1974).

[40] Y.-S. Huang, Y.-J. Tsou, C.-H. Huang, C.-H. Huang, H.-S. Lan, C.-W. Liu, Y.-C. Huang, H. Chung, C.-P. Chang, S.-S. Chu, and S. Kuppurao, IEEE Trans. Electron Devices **64**, 2498 (2017).

[41] Y.-S. Huang, C.-H. Huang, F.-L. Lu, C.-Y. Lin, H.-Y. Ye, I.-H. Wong, S.-R. Jan, H.-S. Lan, C.-W. Liu, Y.-C. Huang, H. Chung, C.-P. Chang, S.-S. Chu, and S. Kuppurao, *2016 IEEE International Electron Devices Meeting (IEDM)* (IEEE, San Francisco, CA, 2016), pp. 33.1.1–33.1.4.

[42] T.-H. Liu, P.-Y. Chiu, Y. Chuang, C.-Y. Liu, C.-H. Shen, G.-L. Luo, and J.-Y. Li, IEEE Electron Device Lett. **39**, 1802 (2018).

[43] J. Liu, X. Sun, D. Pan, X. Wang, L. C. Kimmerling, T. L. Koch, and J. Michel, Opt. Express **15**, 11272 (2007).

[44] S. Gupta, Thesis: Germanium-Tin (GeSn) Technology, Ph.D. thesis, Stanford University, 2013.

[45] W. Dou, Y. Zhou, J. Margetis, S. A. Ghetmiri, S. Al-Kabi, W. Du, J. Liu, G. Sun, R. A. Soref, J. Tolle, B. Li, M. Mortazavi, and S.-Q. Yu, Opt. Lett. **43**, 4558 (2018).

[46] C.-Y. Tsai, C.-H. Chen, T.-L. Sung, T.-Y. Wu, and F.-P. Shih, IEEE J. Quantum Electron. **34**, 552 (1998).

[47] Y. P. Varshni, Phys. Status Solidi B **19**, 459 (1967).

[48] Commissariat à l'énergie atomique et aux énergies alternatives (CEA), Ellipsometry Measure (unpublished).

[49] J. Aubin, J.-M. Hartmann, A. Gassenq, J. L. Rouviere, E. Robin, V. Delaye, D. Cooper, N. Mollard, V. Reboud, and V. Calvo, Semicond. Sci. Technol. **32**, 094006 (2017).

[50] C. Xu, P. M. Wallace, D. A. Ringwala, S. L. Y. Chang, C. D. Poweleit, J. Kouvetakis, and J. Menendez, Appl. Phys. Lett. **114**, 212104 (2019).

[51] S. De Cesari, A. Balocchi, E. Vitiello, P. Jahandar, E. Grilli, T. Amand, X. Marie, M. Myronov, and F. Pezzoli, Phys. Rev. B **99**, 035202 (2019).